

High-Temperature Static Coarsening of Gamma-Prime Precipitates in NiAlCr-X Single Crystals



S.L. SEMIATIN, N.C. LEVKULICH, A.R.C. GERLT, E.J. PAYTON, J.S. TILEY, F. ZHANG, R.A. MACKAY, R.V. MINER, and T.P. GABB

The high-temperature coarsening behavior of γ' precipitates in a series of NiAlCr, NiAlCrTi, NiAlCrW, and NiAlCrTa single-crystal alloys was determined at temperatures between 1158 K and 1473 K (885 °C and 1200 °C). For this purpose, samples were supersolvus solution treated, water quenched, and then subsolvus aged for times between 0.067 and 96 hours. All of the measurements revealed an r^3 dependence of the average precipitate radius on time, thus suggesting bulk-diffusion control of the coarsening process. Coarsening kinetics were fastest for NiCrAl and slowest for NiCrAlTa. The observations were interpreted in terms of the classical Lifshitz–Slyosov–Wagner (LSW) theory modified to account for the finite volume fraction of particles, the composition of the precipitates, and the multicomponent nature of the alloys. By this means, an effective diffusivity for the coarsening process was determined and found to lie between 0.6 and 1.5 times that for the impurity diffusivity of chromium in nickel. Furthermore, the modified LSW theory in conjunction with experimental measurements suggested that the effective diffusivity controlling γ' coarsening at high temperatures in multi-component nickel-base superalloys lay in the lower portion of this range.

<https://doi.org/10.1007/s11661-018-05104-w>

© The Minerals, Metals & Materials Society and ASM International 2019

I. INTRODUCTION

THE thermomechanical processing (TMP) of nickel-base alloys typically focuses on the control of various microstructural features such as the size (and size distribution) of grains, strengthening precipitates, and structure-control phases. The precipitate size/size distribution and volume fraction are particularly important because they affect plastic flow and recrystallization during subsolvus hot working, grain growth following dissolution during supersolvus heat treatment, and mechanical properties such as strength, creep, and fatigue during service.^[1]

A number of phase transformations affect precipitate evolution during TMP. These include (1) dissolution during solution treatment and (2) nucleation, growth, and coarsening during cooling or isothermal subsolvus holding following solution treatment. Because of the

importance of such phenomena, extensive work has been performed to both quantify kinetics and develop descriptive models. For example, the modeling of dissolution has been performed using one of three broad types of approaches, phenomenological,^[2–5] analytical,^[6–8] and phase field.^[9] In addition, the homogeneous nucleation and growth of precipitates have also been treated extensively.^[10–19]

Precipitate coarsening is frequently controlled by bulk diffusion for which the analyses introduced by Lifshitz, Slyosov, and Wagner (“LSW”)^[10,20–23] are usually relied upon to quantify kinetic behavior. Derived for an infinitesimal fraction of precipitates in a two-component system, such approaches have been extended for multi-component alloys with a finite volume fraction of precipitates whose composition is not a terminal solid solution.^[24–31]

Coarsening kinetics and associated models for γ' -strengthened, nickel-base superalloys have received considerable attention in the literature, *e.g.*, the overview by Baldan.^[32] In the vast majority of cases, behavior is controlled by bulk diffusion of solute(s) through the γ matrix, yielding a cubic dependence of the average γ' -precipitate size on time. The corresponding analytical descriptions fall into one of three categories: (i) those which are purely phenomenological in nature,^[33,34] (ii) those based on the LSW analysis without consideration of volume fraction or non-terminal solid-solution effects,^[35–42] and (iii) modified LSW (MLSW) analyses

S.L. SEMIATIN, E.J. PAYTON, and J.S. TILEY are with the Air Force Research Laboratory, Materials and Manufacturing Directorate, Wright-Patterson Air Force Base, OH, 45433. Contact e-mail: sheldon.semiatin.1@us.af.mil N.C. LEVKULICH and A.R.C. GERLT are with UES, Inc., Dayton, OH, 45432. F. ZHANG is with CompuTherm LLC, Middleton, WI, 53562. R.A. MACKAY, R.V. MINER, and T.P. GABB are with the NASA Glenn Research Center, Cleveland, OH, 44135.

Manuscript submitted November 5, 2018.

Article published online February 27, 2019

which incorporate such influences.^[5,43,44] The three different descriptions of coarsening kinetics thus rely on expressions of the following forms to describe the average *three-dimensional* (3D) radius of the γ' precipitates $\bar{R}_{\gamma'}$, $\bar{R}_{\gamma'_0}$ at time t and $t = 0$, respectively:

$$(i) \text{ Phenomenological : } \bar{R}_{\gamma'}^3 - \bar{R}_{\gamma'_0}^3 = K_P(t - t_0) \quad [1]$$

$$(ii) \text{ LSW : } \bar{R}_{\gamma'}^3 - \bar{R}_{\gamma'_0}^3 = \frac{8D\sigma C_{\gamma} V_M}{9RT[1 + \partial \ln v / \partial \ln C_{\gamma}]}(t - t_0) \\ = K_{\text{LSW}}(t - t_0) \quad [2]$$

$$(iii) \text{ MLSW : } \bar{R}_{\gamma'}^3 - \bar{R}_{\gamma'_0}^3 \\ = \frac{8w(\phi)D\sigma C_{\gamma}(1 - C_{\gamma})V_M}{9RT(C_{\gamma'} - C_{\gamma})^2[1 + \partial \ln v / \partial \ln C_{\gamma}]} \\ (t - t_0) = K_{\text{MLSW}}(t - t_0) \quad [3]$$

In these expressions, K_P , K_{LSW} , and K_{MLSW} denote the respective rate constants, D is the effective diffusivity for the rate-limiting solute, σ is the γ - γ' interface energy, C_{γ} and $C_{\gamma'}$ are the equilibrium concentrations of the rate-limiting solute in the matrix and precipitate, respectively, V_M is the molar volume of the precipitate, R is the gas constant, and T is the absolute temperature. The bracketed term in the denominator of Eqs. [2] and [3] is the thermodynamic factor in which v denotes the activity coefficient for the rate-limiting solute in the γ matrix. In Eq. [3], $w(\phi)$ is a factor used to correct for the finite volume fraction ϕ of precipitates. In addition to the diffusivity D (and T in the denominator), various other terms in Eqs. [2] and [3] depend on temperature in a complex fashion. These include $w(\phi)$ (through the dependence of γ' volume fraction on T), C_{γ} , and the thermodynamic factor.

It is important to note that Eqs. [2] and [3] are strictly applicable to binary alloys. Nevertheless, it is usually assumed that similar kinetics follow for multi-component alloys with calculations based on a single, rate-limiting solute. For ternary alloys, on the other hand, the work in Reference 31 revealed that rapidly-diffusing solutes also influence the rate of coarsening. In the general case, it may be surmised that an effective rate constant (K_{eff}) equal to the inverse of the sum of the inverse rate constants for each of the individual solutes can be defined as the following:

$$\frac{1}{K_{\text{eff}}} = \frac{1}{K_1} + \frac{1}{K_2} + \frac{1}{K_3} + \dots \quad [4]$$

It is also implicitly assumed in Eqs. [1] through [3] that the precipitate distribution is uni-modal. This restriction has been relaxed in several numerical approaches designed to treat the coarsening of γ' distributions that are bimodal.^[45,46] Such distributions

may be developed during isothermal subsolvus heat treatment at two temperatures or supersolvus solution treatment following by continuous cooling. During the latter instance, precipitate nucleation and growth often occur in two “bursts”, one at high temperatures (producing secondary γ') and the other at a much lower temperature (yielding tertiary γ').

The objective of the present work was to explore the applicability of the modified LSW model for the description of coarsening in multi-component superalloys with special attention to several factors often not treated in sufficient detail, *i.e.*, the compositions of the matrix and precipitate, the volume-fraction factor, and stereological methods used to relate two-dimensional (2D) precipitate sizes measured on polished sections to the actual 3D radii in expressions such as Eqs. [1] through [3]. For this purpose, MLSW model predictions were first compared to experimental observations of the coarsening behavior of γ' in several NiAlCrX model (single-crystal) alloys; this enabled the direct evaluation of the effect of different quaternary elements on coarsening of a baseline NiAlCr ternary superalloy. These results were then compared to prior observations for various commercial powder-metallurgy superalloys containing greater numbers of elements.

II. MATERIALS AND PROCEDURES

A. Materials

Various ternary and quaternary nickel-base alloys were used in the present work to establish the coarsening behavior of materials which are less complex than commercial superalloys, thus providing insight into possible solute-interaction effects. Specifically, the program materials comprised single crystals denoted as NiAlCr, NiAlCrTi, NiAlCrW, and NiAlCrTa. They were received as remnants of slabs that had been cast by General Electric Aircraft Engines (Evendale, OH), solution treated, and aged for a prior research program dealing with deformation behavior performed at NASA Lewis Research Center (now NASA Glenn Research Center) in the 1990s.^[47] The bulk composition of each alloy in atomic fraction (*a/o*), determined by GE, is summarized in Table I. The (average) composition of the γ' phase (Table II) was determined by NASA *via* electrolytic extraction. As suggested by the results in Reference 36, the temperature dependence of the composition of γ' for each of the present alloys is likely

Table I. Ni SX Compositions (a/o) and Room-Temperature Lattice Mismatch δ ^[47]

Alloy	Al	Cr	X	δ (Pct)
NiAlCr	14.3	10.0	—	0.067
NiAlCrTi	12.9	10.2	1.8	0.169
NiAlCrW	12.9	10.0	2.1	0.143
NiAlCrTa	13.6	9.9	1.6	0.359

$\delta = 2(a_{\gamma'} - a_{\gamma})/(a_{\gamma'} + a_{\gamma})$, in which a denotes the stress-free lattice parameter.

Table II. γ' Compositions in Ni SX's (a/o)^[47]

Alloy	Al	Cr	X
NiAlCr	18.4	7.8	—
NiAlCrTi	17.3	6.3	2.5
NiAlCrW	18.1	5.0	3.1
NiAlCrTa	18.0	5.7	2.9

small. The influence of a small temperature dependence on predicted coarsening rates would likely be limited in view of the noticeable partitioning of the various alloying elements between the γ and γ' phases and the importance of the *difference* in phase composition (as exemplified by term $(C_{\gamma'} - C_{\gamma})^2$ in the denominator in Eq. [3]).

B. Experimental Procedures

A number of small sections, each measuring approximately $5 \times 5 \times 10$ mm were extracted from the single-crystal alloys *via* electric-discharge machining (EDM); one of the 5-mm dimensions was parallel to the $\langle 001 \rangle$ solidification direction of the corresponding slab. Samples of each alloy were encapsulated in quartz tubes that had been evacuated and backfilled with argon and first supersolvus solution treated for 1 hour at 1503 K (1230 °C) (NiAlCr) or 1533 K (1260 °C) (the three quaternary alloys) followed by water quenching. Each sample was then re-encapsulated in a similar manner followed by coarsening heat treatment at a temperature between 1158 K and 1473 K (885 °C and 1200 °C) for a time between 0.067 and 96 hours followed by water quenching.

Coarsening behavior was established using images taken in a scanning electron microscope (SEM). For this purpose, each heat-treated sample was sectioned along a plane perpendicular to the solidification direction and prepared using standard procedures. Metallographic preparation comprised grinding with SiC papers down to 800 grit, rough polishing with diamond, final polishing with colloidal silica, and etching in a solution of 33 pct nitric acid, 33 pct glacial acetic acid, 33 pct deionized water, and 1 pct hydrofluoric acid.

The area fraction of γ' was determined *via* point counting on secondary-electron (SE) or backscatter electron (BSE) micrographs taken at magnifications between 5 and 100 kX using a Zeiss Gemini SEM or FEI Quanta SEM, respectively. SE imaging was performed using an accelerating voltage of 0.5 kV, working distance between 3 and 4 mm, and aperture size of 20 μm . BSE imaging was conducted using an accelerating voltage of 20 kV, working distance of 10 mm, spot size of 5, and aperture size of 30 μm . At least 2 typical images (superimposed with ~ 3000 point-count grid intersections) were used for each test condition/imaging method. Only one-half of the point-count intersections lying on halos were counted for SE images with such features. For the BSE images, particles lying under the section plane were manually eliminated during point counting because of the ambiguity introduced by the

finite penetration depth of the electron beam, an effect quantified by comparing BSE and SE images.

The number of precipitates per unit area was also determined manually for each heat-treatment condition. From the precipitate area fraction and number-density results, an *approximate* two-dimensional (2D) circle-equivalent diameter (CED) was determined; the uncertainty in this quantity was estimated to be less than 5 pct of the values reported below. It should be noted that this technique yielded a value of the *diameter of the average precipitate area*, herein denoted as d_a .

The manually-determined values of area fraction and d_a were compared to results from automated image analysis (using the MIPAR software^[48,49]) on selected micrographs that enabled reliable segmentation of the γ and γ' phases. This method provided the area fraction and complete 2D CED size distribution as well as the *average* CED of the precipitates in the 2D section (\bar{d}) and its standard deviation.

The experimental measurements were complemented by a stereology investigation used to correlate 2D metallographic observations and actual 3D features pertinent to coarsening models such as the “caliper” diameter.^[50] For this purpose, a number of hypothetical distributions of spherical particles, each with a specified volume fraction and standard deviation, were instantiated into a cubic box using Python. For each instantiation, a number of arbitrarily-oriented planar sections through the box was taken, and the average diameter of the 2D circular sections through the ensemble of particles (\bar{d}) was determined and compared to the average 3D diameter (\bar{D}). These simulations also provided a relation between \bar{d} and d_a for the precipitates in 2D sections. The results of importance with regard to the present work were thus twofold: (1) The dependence of the ratio \bar{d}/d_a on the standard deviation “ s ” of the 2D d/\bar{d} distribution and (2) the transfer function, κ_d , representing the ratio of the average 3D caliper diameter (\bar{D}) to the value of \bar{d} as a function of “ s ”. Figure 1 illustrates these quantities for assumed 3D lognormal distributions of spherical volumes. In such cases, the results revealed that \bar{d}/d_a is always *less* than unity (Figure 1(a)), and $\kappa_d = \bar{D}/\bar{d}$ decreases from values greater than unity for small 2D standard deviations s to values less than unity for large s (Figure 1(b)). However, the simulation plots indicated that the functional dependence on s of \bar{d}/d_a and κ_d was each essentially linear.

III. RESULTS

The principal results of this investigation comprised SEM observations of the precipitate structures, corresponding quantitative metallography, and determination of coarsening rates.

A. Precipitate Observations

Typical examples of the precipitate distributions developed during heat treatment of the four NiAlCrX alloys at 1353 K and 1158 K (1080 °C and 885 °C) are

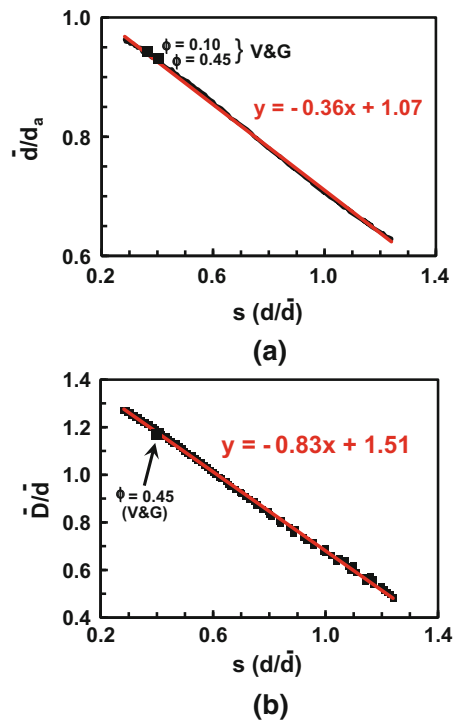


Fig. 1—Stereology results for assumed lognormal distributions of spherical precipitate particles: (a) ratio of the average 2D diameter (\bar{d}) to the diameter of the average 2D area (d_a) as a function of the standard deviation s of the 2D d/\bar{d} distribution and (b) ratio κ_d of the average 3D (caliper) diameter (\bar{D}) to the average 2D diameter (\bar{d}) as a function of s .

shown in Figures 2, 3, 4, 5, 6, 7, 8, and 9. At the higher temperature (Figures 2, 3, 4, 5), the precipitates in each case were largely circular in 2D section after short (0.067 hour) and intermediate (8 hour) times. At the longest time (96 hours), the precipitates were either circular (NiAlCrTi) or had begun a transition to a square/cuboidal-like shape (NiAlCr, NiAlCrW, NiAlCrTa). At 1158 K (885 °C), the volume fraction of precipitates was noticeably higher for each alloy (Figures 6, 7, 8, 9). In most cases, the precipitates retained a predominantly-circular shape in 2D sections, but there was some evidence of precipitate coalescence, especially at the longest time of 72 hour (*viz.*, NiAlCr, NiAlCrTa). The fraction of coalesced particles relative to total particles at 1158 K (885 °C) lay in the range between 1 and 12 pct. When quantifying coarsening behavior in these instances, each coalesced entity was counted as two (or three) particles in the estimation of the average particle size.

Measurements of area fraction (\sim volume fraction) indicated no discernible dependence on heat-treatment time. For a given alloy/temperature, the volume fraction variation in almost all cases was within ± 0.02 , and often within ± 0.01 of the average for all times, thus suggesting that a near-equilibrium state had been established, except for the very small change typically associated with coarsening itself (< 0.01). Based on these observations, plots of the volume fraction of γ' as a function of temperature (*i.e.*, solvus-approach curves) were constructed (Figure 10). Each of these curves had a

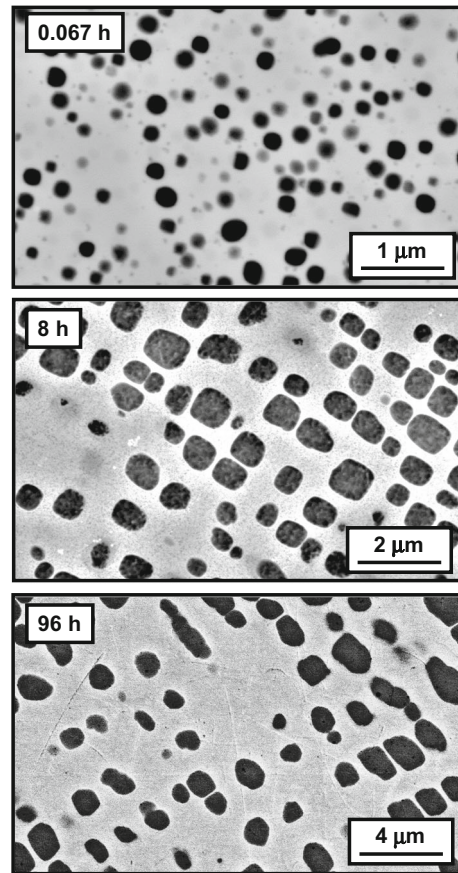


Fig. 2—SEM BSE images illustrating the coarsening of γ' precipitates in NiAlCr single crystals at 1353 K (1080 °C).

shape reminiscent of that typically observed for commercial PM nickel-based superalloys^[51]; *i.e.*, a steep increase in fraction with decreasing temperature near the solvus temperature (at which fraction $\gamma' = 0$) and a relatively-shallow temperature dependence several hundred degrees Kelvin below the solvus. The plots also revealed that the solvus temperature was lowest for the NiAlCr alloy and highest for NiAlCrTa. The NiAlCr alloy also had the lowest measured area fraction of γ' at comparable heat-treatment temperatures.

B. Quantitative Metallography and Coarsening Rates

Measured (2D) particle-size distributions (examples of which are shown in Figure 11) revealed slightly-asymmetric patterns skewed to the left of $d/\bar{d} = 1$ (or equivalently $r/\bar{r} = 1$) with a maximum particle size of approximately $d_{\max} \sim (1.7 \text{ to } 2)\bar{d}$. Furthermore, the standard deviation of the histograms for which the abscissa is normalized as d/\bar{d} lay between approximately 0.30 and 0.40. The present distributions were similar to those deduced from the 3D results of Voorhees and Glicksman (V&G),^[27] the latter converted from 3D to 2D (Figure 12) using the ‘balls-in-a-box’ approach described briefly in Section II.B and in more detail in Reference 52. There were some differences between the measured and V&G 2D size distributions, however,

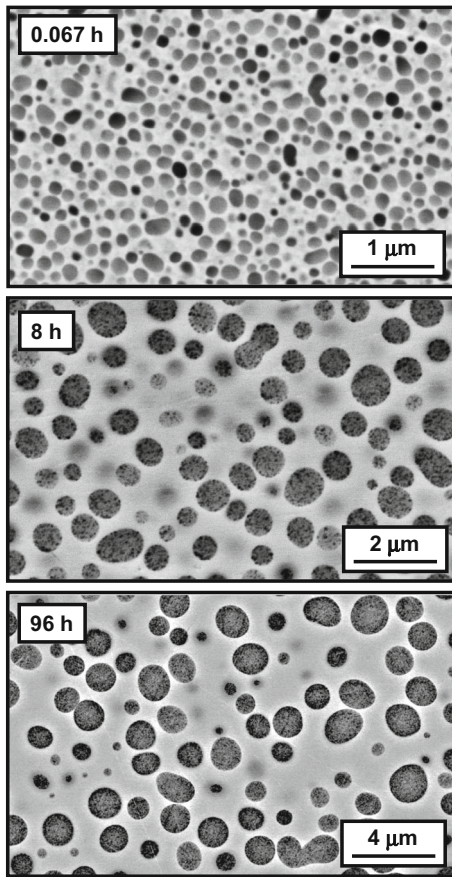


Fig. 3—SEM BSE images illustrating the coarsening of γ' precipitates in NiAlCrTi single crystals at 1353 K (1080 °C).

primarily at small particle sizes (Figure 11). Such variations were likely an artifact of the moderate magnifications used to image a large number of particles, thus obscuring the low end and producing somewhat larger-than-actual peaks in the measured distributions. Nevertheless, the V&G simulations did indicate that the normalized standard deviation of the size distributions for the various volume fractions was in the range of 0.36 to 0.40 in 2D, similar to that found experimentally, or 0.39 to 0.40 in 3D.

The V&G 2D distributions also revealed that the dependence of \bar{d}/d_a on the standard deviation s of the 2D diameters followed the same trend as that for lognormal distributions, albeit the range of \bar{d}/d_a lay within a relatively-narrow window (0.944 to 0.930) for volume fractions of precipitate between 0.1 and 0.45 (Figure 1(a)).

To avoid the difficulty associated with the thresholding/segmenting of a large number of micrographs, the coarsening kinetics of the four single-crystal alloys was quantified using values of d_a derived from point-counted area fraction and number-per-unit-area measurements. These data were converted to average diameter \bar{d} (and thence to average 2D radii \bar{r}) using a value of $\bar{d}/d_a = 0.938$, corresponding to the average 2D standard deviation of both the measured 2D size distributions and the 2D V&G distributions, *i.e.*, ~ 0.38 (Figure 1(a)). Typical

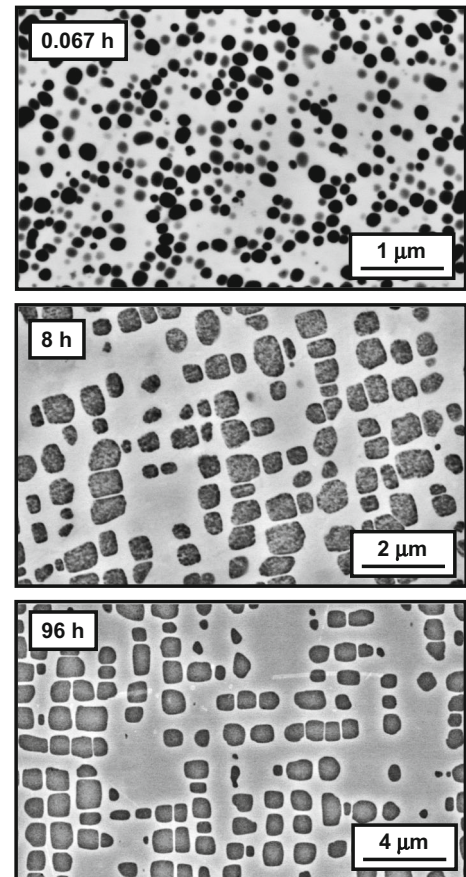


Fig. 4—SEM BSE images illustrating the coarsening of γ' precipitates in NiAlCrW single crystals at 1353 K (1080 °C).

results for the four alloys at two different temperatures (Figure 13) revealed that coarsening kinetics followed \bar{r}^3 vs t behavior. The slopes of the various lines indicated that the coarsening rate constant (K) was lowest for the NiAlCrTa alloy and increased successively for NiAlCrW, NiAlCrTi, and NiAlCr at both temperatures. A similar alloy-dependence of the rate constant was exhibited for the balance of the measurements as shown in the summary plot in Figure 14. No attempt was made to derive an apparent activation energy from the data in this figure because of the complex nature of the temperature dependence of the various terms in the modified LSW coarsening expression (Eq. [3]). These dependences are discussed in more detail in the next section.

IV. DISCUSSION

All measurements of the rate of coarsening of γ' precipitates in the NiAlCr, NiAlCrTi, NiAlCrW, and NiAlCrTa alloys indicated a cubic dependence of average radius on time, similar to prior investigations for a number of nickel-base superalloys. In this section, these observations are interpreted in the context of the modified LSW relation (Eq. [3]). The various input parameters are first summarized. Subsequently,

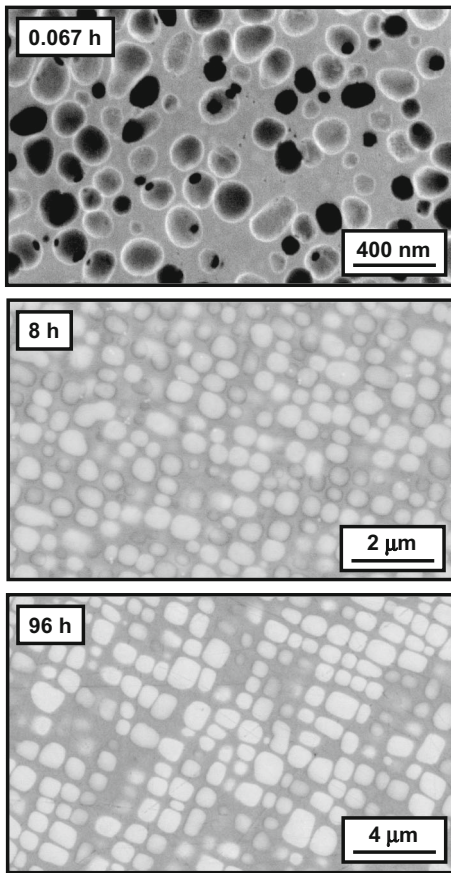


Fig. 5—SEM micrographs illustrating the coarsening of γ' precipitates in NiAlCrTa single crystals at 1353 K (1080 °C). The micrograph for the shortest time is an SE image, while those for the two longer times are BSE images.

theoretical estimates based on both a rate-limiting solute as well as all solutes are compared to the 2D rate constants and values corrected for 2D-to-3D stereology. Literature measurements of the coarsening rate for commercial alloys are then compared to MLSW model predictions.

A. Input Data for Coarsening Analysis

The material/model parameters needed for the coarsening analysis consisted of the phase compositions (C_γ , $C_{\gamma'}$), molar volume of the precipitate (V_M), thermodynamic factors, precipitate-matrix interface energy (σ), volume-fraction function ($w(\phi)$), and effective diffusivity for the various solutes (D_{eff}).

The phase compositions at a given temperature were based on the measured (average) composition of γ' determined previously by phase extraction^[47] (Table II), the volume fraction measurements (summarized in the solvus-approach curves, Figure 10), and a simple mass balance. The resulting “composition factors” in Eq. [3], *i.e.*, $[(C_\gamma(1 - C_\gamma)/(C_{\gamma'} - C_\gamma)^2]$, showed a marked dependence on alloy, alloying element, and temperature (Figure 15). Equally, if not more, important is the fact that in many cases the magnitude of the composition factor lay in the range of 10 to 300. Thus, simple

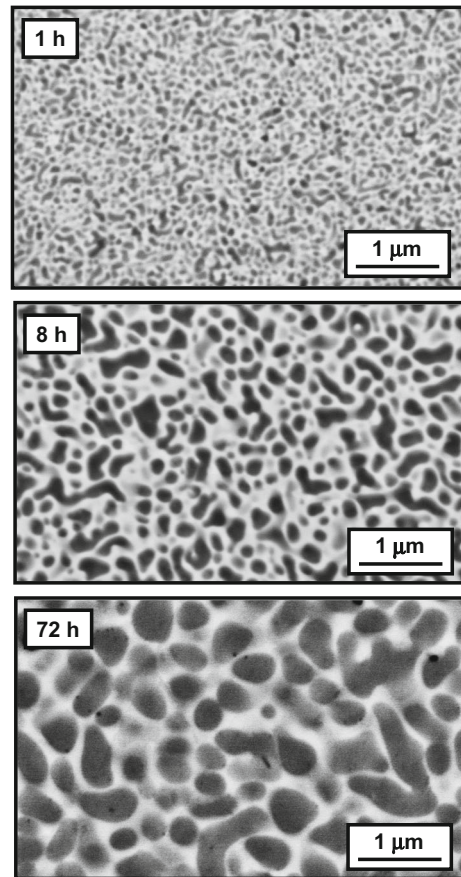


Fig. 6—SEM BSE micrographs illustrating the coarsening of γ' precipitates in NiAlCr single crystals at 1158 K (885 °C).

analyses for the rate constant (*e.g.*, Eq. [2]), which disregard the composition factor, can be expected to provide predictions that are low by one or two orders of magnitude.

The molar volume of the precipitate in the alloys was estimated based on the gram molecular weight and an approximate precipitate density of 8000 kg/m³. This yielded V_M values between 6.5×10^{-6} m³ and 7×10^{-6} m³. Because of uncertainty in the precipitate density, a fixed V_M of 6.75×10^{-6} m³ was used for all alloys. The thermodynamic factors were estimated using the Pandat[®] software. These values showed a moderate dependence on alloy composition and temperature, but were generally in the range of 1.6 to 3.7 (Al), 1.3 to 2 (Cr), 1.1 to 1.6 (Ti), 1 to 1.25 (W), and 1 to 1.4 (Ta). The thermodynamic factor increased with temperature for Al, Ti, W, and Ta and decreased with temperature for Cr.

The value of the interface energy σ was taken from literature estimates based on the temperature at which precipitate nucleation occurs during cooling following supersolvus solution treatment; at this temperature, the decrease in volumetric free energy is exactly balanced by the increase in surface energy. An analysis of this sort for several commercial superalloys has suggested that σ is between 23 and 25 mJ/m².^[51] This value is comparable to that reported by Baldan,^[32] *i.e.*, 21.3 mJ/m², and

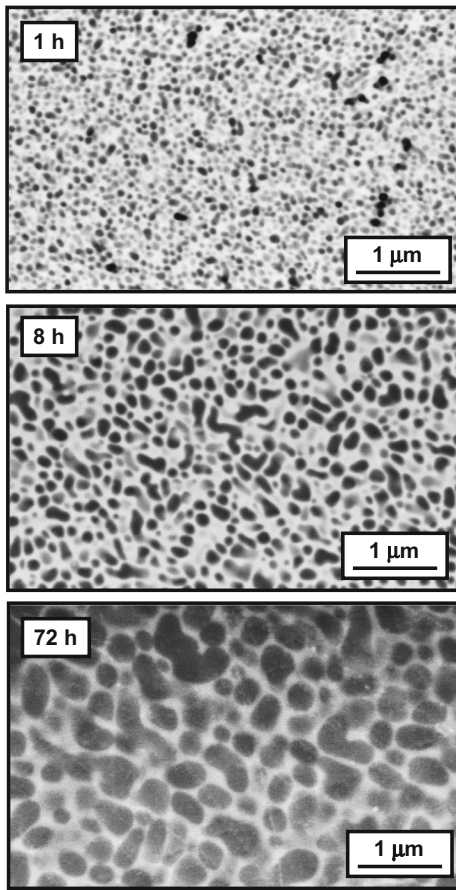


Fig. 7—SEM BSE micrographs illustrating the coarsening of γ precipitates in NiAlCrTi single crystals at 1158 K (885 °C).

Sudbrack *et al.*^[52] *i.e.*, 22 to 23 mJ/m². In the present work, a fixed value of 23 mJ/m² was therefore used.

Of the various approaches to quantify the volume fraction dependence of the coarsening rate constant, $w(\phi)$, that due to Voorhees and Glicksman^[26,27] appears to provide the most reasonable estimate, as suggested by coarsening data for Ti-6Al-4V in the literature.^[53] For $0.1 \leq \phi \leq 0.7$, the following approximate analytical form was thus fit to provide a tradeoff between experimental measurements and the Voorhees-and-Glicksman predictions (Figure 16):

$$w(\phi) = 13.2\phi^2 - 3.01\phi + 1.992 \quad [5]$$

The diffusivity in Eq. [3] represents perhaps the most difficult parameter to quantify for multi-component systems. Because coarsening rates were predicted based on both a rate-limiting solute as well as all solutes, it was necessary to estimate effective diffusivities for Al, Cr, Ti, W, and Ta. For this purpose, the diffusivity of Cr in the binary Ni-Cr system^[54] was used as a baseline with a constant (“tuning”) factor A utilized to adjust for the influence of other solutes for a given alloy system, *i.e.*,

$$\begin{aligned} D_{\text{eff Cr}}(\text{m}^2/\text{s}) &= A \times D_{\text{Ni-Cr}} \\ &= A \times 0.00036 \exp(-34278/T(\text{K})) \quad [6] \end{aligned}$$

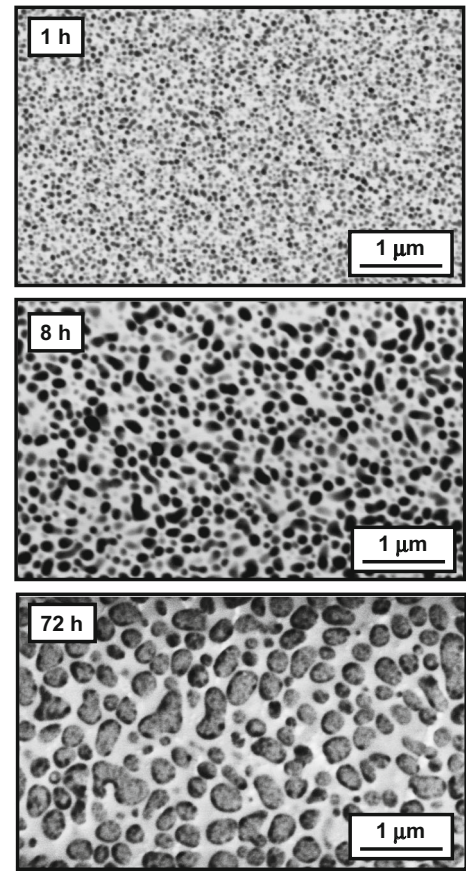


Fig. 8—SEM BSE micrographs illustrating the coarsening of γ precipitates in NiAlCrW single crystals at 1158 K (885 °C).

The value of A , whose magnitude was of the order of unity, was chosen to provide the best match between measured and predicted coarsening rates over the temperature range of interest. To estimate the effective diffusivity of the other solutes, Rene88/alloy 718 diffusion-couple data at 1423 K (1150 °C)^[55] (Table III) were used. Specifically, the ratio of the diffusivity of a given solute to that of Cr was taken to be the same as that from these former measurements. This ratio was assumed to be independent of temperature in view of the similarity in diffusion activation energy (*viz.*, ~ 285 kJ/mol) commonly observed for Ni-X binary alloys.^[54] The tantalum solute, for which no data are available in Reference 55 (or elsewhere), was assumed to have a diffusivity equal to that of chromium.

B. Comparison of Measured and Predicted Rate Constants

A comparison of measured and predicted coarsening-rate constants (Table IV, with values plotted in terms of nm³/s) quantified the importance of the interaction of different solutes in a given alloy, stereological factors to convert 2D to 3D measurements, and the limitations of the modified LSW model at high volume fractions of precipitate. In line with the plot in

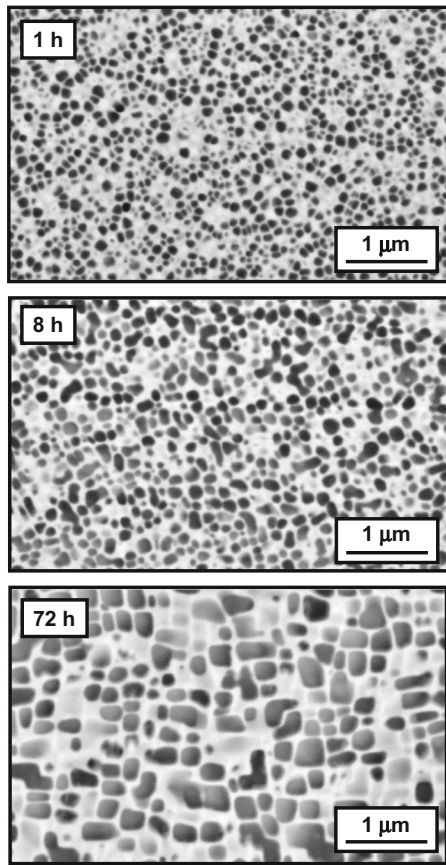


Fig. 9—SEM BSE micrographs illustrating the coarsening of γ' precipitates in NiAlCrTa single crystals at 1158 K (885 °C).

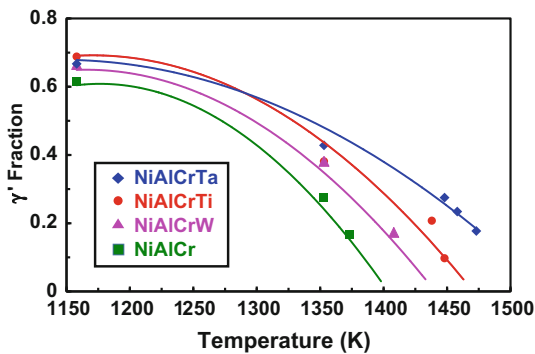


Fig. 10—Measured area fractions of γ' precipitates (data points) and approximate solvus-approach curves for the NiAlCrX single crystal alloys (Color figure online).

Figure 14, the *measured* 2D values for each alloy (third column of the table, denoted as K for brevity) exhibited a 2 to 3 order-of-magnitude variation over the temperature range investigated. One might conclude that such a variation is primarily due to the temperature dependence of the effective diffusivity. Per Eq. (6), the diffusivity does increase by a factor of approximately 500 between 1158 K and 1473 K (885 °C and 1200 °C). However, the import of other material coefficients is obscured by their different dependences on temperature. In particular, the composition factor *increases* with

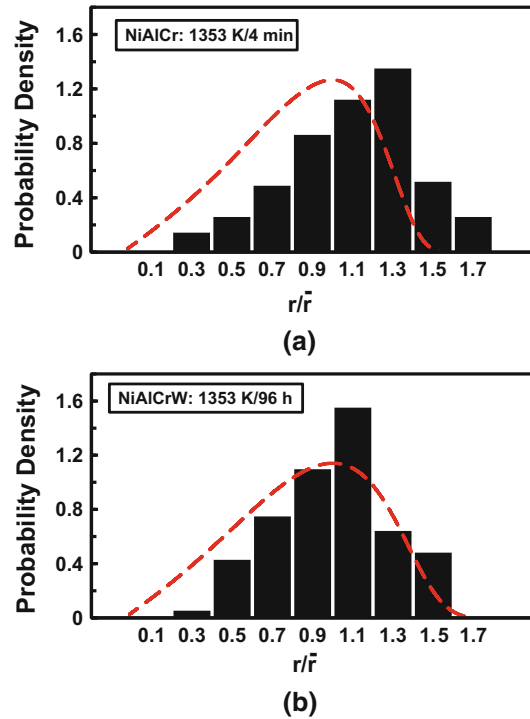


Fig. 11—Examples of the 2D size distributions determined by image analysis using MIPAR software: (a) NiAlCr heat treated at 1353 K (1080 °C) for 4 min or (b) NiAlCrW heat treated at 1353 K (1080 °C) for 96 h. The measurements are compared to simulation results (red broken lines) from Voorhees and Glicksman^[27] which have been converted to 2D (Color figure online).

increasing temperature and the function $w(\phi)$ *decreases* with temperature as the volume fraction decreases.

In the fourth and fifth columns of Table IV, two sets of model predictions of the rate constant are summarized: One based solely on the solute whose value of K is lowest (*i.e.*, the rate-limiting solute, RLS) and the other based on all the solutes per Eq. [4]. Note that all entries in these two columns have been normalized by the coefficient A in Eq. [6]. The calculations for the various alloys revealed that no single alloying element controls the coarsening behavior in all cases, although Cr was found to be the RLS more often than other elements with Al being the second most common. Furthermore, by analogy with “parallel” electric circuits, the value of K_{eff} derived from Eq. [4] when all solutes are considered is always less than that for any individual element. In the extreme case for which the values of K of the non-rate-limiting solutes are only slightly greater than that of the RLS, K_{eff} would be approximately one-half or one-third that of the RLS in a ternary or quaternary alloy, respectively. Hence, it is not surprising that a number of instances in Table IV do indeed show that the K derived considering all of the alloying elements is *lower* in comparison to the RLS estimate by a factor in the range of 1.5 to 3.

The final two columns in Table IV provide estimates of the coefficient A in Eq. [6], derived by dividing the measured value of K in column 3 (with or without a stereological correction to obtain the pertinent 3D quantity) by model predictions (normalized by A). For

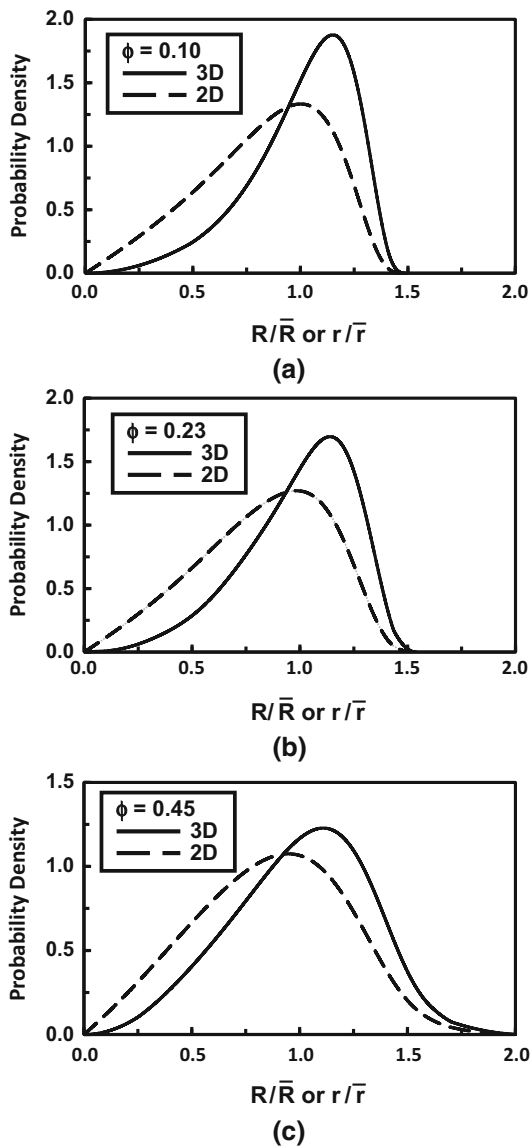


Fig. 12—Comparison of 2D and 3D normalized particle-size distributions for the coarsening of a dispersion of precipitates having a volume fraction of either (a) 0.1, (b) 0.23, or (c) 0.45. The 3D distributions come from the work of Voorhees and Glicksman^[27]

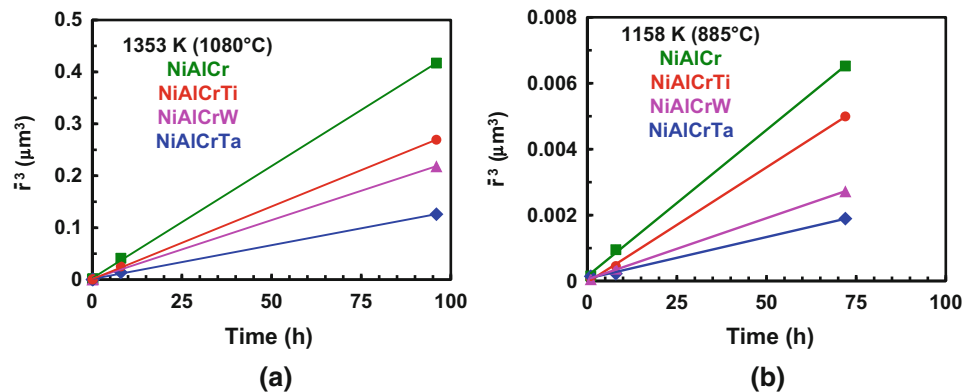


Fig. 13—2D coarsening kinetics in terms of \bar{r}^3 as a function of time at (a) 1353 K (1080 °C) or (b) 1158 K (885 °C). Green/squares—NiAlCr, red/circles—NiAlCrTi, pink/triangles—NiAlCrW, blue/diamonds—NiAlCrTa (Color figure online).

the present precipitate-size distributions, the 2D standard deviation was ~ 0.4 yielding $\kappa_d = \bar{D}/\bar{d} \sim 1.18$ (Figure 1(b)). The stereological correction to r^3 and the measured 2D coarsening rate constant was thus $1.18^3 = 1.64$, *i.e.*, a relatively-substantial quantity. Using the stereologically-corrected measurements and model predictions based on all of the alloying elements, the value of A was found to lie in a relatively-narrow range between approximately 0.6 and 1.5 for all of the test conditions, except those for the lowest temperature, 1158 K (885 °C). Thus, in most cases, the effective diffusivity for Cr was comparable to that for chromium in nickel.

In contrast to the findings at higher temperatures, the values of A at 1158 K (885 °C), were much larger for the NiAlCr, NiAlCrTi, and NiAlCrW alloys. Such a finding may be attributable to (1) the large volume fraction of precipitates (≥ 0.6) at this temperature and the fact that the function $w(\phi)$ changes very rapidly with ϕ and thus may not be accurate and/or (2) the contribution of particle coalescence to coarsening which has not been taken into account. With regard to the former influence, the highest values of A (~ 4 to 5) were found for NiAlCrTi and NiAlCrW for which the volume fraction

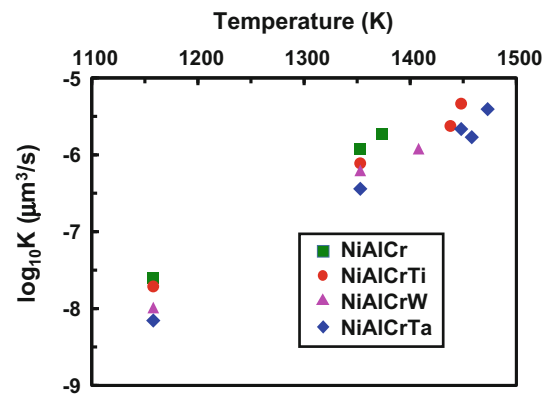


Fig. 14—Summary of measured 2D coarsening rate constants as a function of temperature. Green/squares—NiAlCr, red/circles—NiAlCrTi, pink/triangles—NiAlCrW, blue/diamonds—NiAlCrTa (Color figure online).

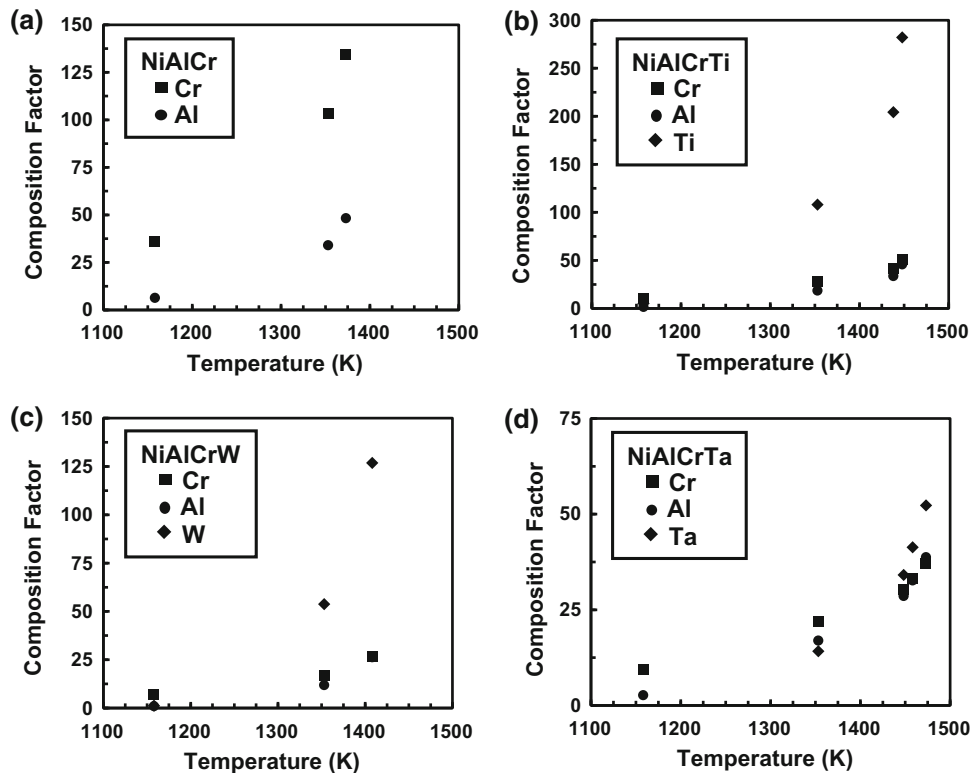


Fig. 15—The temperature dependence of the composition factor for the solutes in (a) NiAlCr, (b) NiAlCrTi, (c) NiAlCrW, (d) NiAlCrTa.

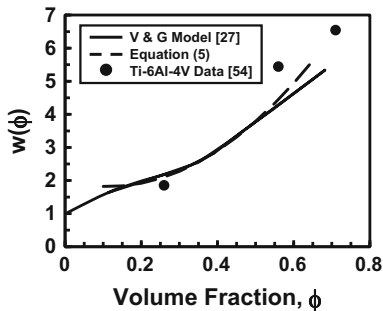


Fig. 16—Comparison of the Voorhees-and-Glicksman model prediction^[27] of the volume-fraction factor for the coarsening rate constant, experimental measurements for Ti-6Al-4V,^[54] and an analytical fit for $0.1 \leq \phi \leq 0.7$.

Table III. Diffusivity Data from Rene88/Alloy 718 Diffusion Couple Heat Treated at 1423 K (1150 °C)^[55]

Element	$D \times 10^{15} \text{ (m}^2\text{/s)}$	D/D_{Cr}
Cr	1.92	1.0
Al	5.89	3.07
Co	9.41	4.90
Fe	3.87	2.02
Mo	3.61	1.88
Nb	4.11	2.14
Ti	4.48	2.33
W	3.02	1.57

was in the range 0.65 to 0.70. For NiAlCr at 1158 K (885 °C), the volume fraction was slightly lower, but still somewhat high (*i.e.*, 0.61). The value of A for NiAlCrTa at this temperature contrasted with the other values despite its high volume fraction (0.67), and thus warrants further investigation.

C. Effect of Precipitate-Matrix Lattice Mismatch on Coarsening Rate

It has been suggested that increasing magnitudes of the mismatch δ in the lattice parameters of the γ' and γ phases (*e.g.*, δ from -0.1 to -0.7 pct) can noticeably decrease the coarsening rate, especially for long-times (1000's of hours) at high temperatures.^[56] The present single-crystal alloys had relatively-small levels of positive lattice mismatch at room temperature (Table I).^[47] After decreasing these values by ~ 0.17 pct to account for the often-observed decrement in mismatch from room temperature to ~ 1373 K (1100 °C),^[47,57] the high-temperature values of δ would be slightly negative (-0.1 pct) for NiAlCr, almost zero for NiAlTi and NiAlW, and slightly positive ($+0.2$ pct) for NiAlCrTa. Thus, the magnitudes of δ for the present single-crystal alloys (*i.e.*, ≤ 0.2 pct) were substantially less than the maximum values exhibited by the alloys in Reference 56. Hence, it can be surmised that lattice mismatch likely played a minor role in the present coarsening observations.

Table IV. Comparison of Measured and Predicted Coarsening Rate Constants

Alloy	Temp (K)	2D Meas K (nm ³ /s)	3D Pred K/A (RLS) (nm ³ /s)	3D Pred K/A All Elem (nm ³ /s)	A = Meas (No Stereo)/ Pred (All Elem)	A = Meas (w/Stereo)/ Pred (All Elem)
NiCrAl	1158	24.6	28.4 (Al)	21.4	1.15	1.88
NiCrAl	1353	1199.7	2779 (Al)	1989	0.60	0.99
NiCrAl	1373	1850.3	4609 (Al)	3274	0.57	0.93
NiCrAlTi	1158	19.4	12.8 (Al)	7.1	2.73	4.49
NiCrAlTi	1353	776.9	2335 (Cr)	1093	0.71	1.17
NiCrAlTi	1438	2377.2	11,400 (Cr)	5441	0.44	0.72
NiCrAlTi	1448	4635.2	15,314 (Cr)	7707	0.60	0.99
NiCrAlW	1158	10.3	8.9 (W)	3.5	2.94	4.84
NiCrAlW	1353	627.5	1439 (Cr)	695	0.90	1.48
NiCrAlW	1408	1208.2	4216 (Cr)	2208	0.55	0.90
NiCrAlTa	1158	7.0	17.1 (Al)	14.3	0.49	0.80
NiCrAlTa	1353	361.6	1505 (Ta)	617	0.59	0.96
NiCrAlTa	1448	2171.5	10,496 (Cr)	3868	0.56	0.92
NiCrAlTa	1458	1699.2	12,611 (Cr)	4808	0.35	0.58
NiCrAlTa	1473	3929.0	16,669 (Cr)	6644	0.59	0.97

Table V. Coarsening Behavior for Multi-component γ - γ' Superalloys

Alloy	Temp (K)	2D Meas K (nm ³ /s)	3D Pred K/A RLS* (nm ³ /s)	3D Pred K/A All Elem (nm ³ /s)	A = Meas (No Stereo)/ Pred (All Elem)	A = Meas (w/Stereo)/ Pred (All Elem)
LSHR	1033	0.0069**	0.189	0.0833	0.082	0.082
LSHR	1116	0.422**	2.09	1.06	0.40	0.40
LSHR	1200	3.38	17.4	9.63	0.35	0.58
LSHR	1366	99	549	345	0.29	0.47
Alloy	1116	0.367**	2.71	1.39	0.26	0.26
10	1200	5.11	23.0	12.7	0.40	0.66
	1366	183	697	432	0.42	0.70
IN-100	1373	299	1479	469	0.64	1.04
Rene88	1273	18.1	77.1	28.9	0.63	1.03

*In all cases, Cr is the rate-limiting solute (RLS).

**No stereological correction needed for 2D \rightarrow 3D because all measurements came from TEM foils. All other 3D data inferred using stereological correction of 1.18.

D. Measured and Predicted Rate Constants for Multi-component Alloys

A comparison of measured and predicted coarsening-rate constants for multi-component powder-metalurgy (PM) γ - γ' superalloys exhibited a similar behavior to the model single-crystal alloys. Attention was focused on 4 materials (LSHR, Alloy 10, IN-100, and Rene 88), which were coarsened at temperatures at which the volume fraction of γ' was equal to or less than ~ 0.5 . The coarsening data came from References 51 and 58, which also contained the overall alloy and γ' phase compositions. The bulk of the prior measurements employed SEM observations on 2D metallographic sections. For several of the PM superalloys heat treated at relatively-low temperatures, however, the microstructure was too fine to discern *via* SEM, and transmission electron microscopy (TEM) was therefore used to determine precipitate sizes. In TEM, the entire 3D precipitate cross section is imaged, and hence no

stereological correction is needed to interpret measured rate constants.

Measured rate constants for the multi-component PM superalloys are summarized in the third column of Table V. The corresponding predictions based on a rate-limiting solute (RLS) or on all of the alloying elements are shown in the fourth and fifth columns. As for the single-crystal alloys, the predictions based on all of the elements in a given alloy were approximately one-half to one-third of those based on the rate-limiting solute. The ratio of the measured rate constants (with-out or with a stereological correction of 1.18 for converting 2D average radii to 3D) to the model predictions based on all solutes again provided estimates of the coefficient *A* in Eq. [6]. As expected, including the stereological correction to the measurements (except for those based on TEM) yielded a value of *A* which was 65 pct higher ($\sim 1.18^3 - 1$) than those not corrected for stereology. The final column of Table V, summarizing

the values of A for which the measurements were corrected for stereology (where appropriate), indicated trends which were similar to those found for the single-crystal alloys (Table IV). Specifically, values of A equal to approximately unity were found for the two second-generation PM superalloys, IN-100 and Rene 88. For the third-generation PM superalloys (LSHR and Alloy 10, each with generally-higher levels of refractory additions), A was lower, generally in the range of 0.4 to 0.7, except for two of the cases. The source of the low value of A for Alloy 10 heat treated at 1116 K (843 °C) is unknown. By contrast, the low value of A for LSHR coarsened at 1033 K (760 °C) was likely due to a transition from coarsening controlled by bulk diffusion of solutes through the γ matrix to one limited by diffusion of refractory solutes across matrix-precipitate interfaces, *i.e.*, so-called trans-interface diffusion control.^[59]

V. SUMMARY AND CONCLUSIONS

A series of model superalloy single crystals (NiAlCr, NiAlCrTi, NiAlCrW, NiAlCrTa) was supersolvus solution treated and then subsolvus annealed to establish the kinetics of γ' coarsening of precipitates. The following conclusions were drawn from this work:

1. All of the alloys exhibit a cubic dependence of the average particle radius on time. At a given temperature, the coarsening rate is fastest for NiAlCr and progressively decreases for NiAlCrTi, NiAlCrW, and NiAlCrTa.
2. The temperature dependence of the rate constant for the coarsening of γ' in nickel-base superalloys is confounded by the specific dependences on the effective diffusivity and concentration factor, both of which *increase* with temperature, and the volume-fraction function which decreases with increasing temperature.
3. A modified LSW analysis of experimental data for the NiAlCrX alloys has demonstrated the importance of incorporating the influence of all solutes on coarsening predictions as well as taking proper account of the stereology of 2D vs 3D microstructural observations. In particular, the predicted rate constant is reduced by a factor of 2 to 3 when all of the solutes are considered rather than merely that which appears to be rate limiting. For precipitate distributions developed during coarsening, the stereological factor needed to convert the average 2D radius to the corresponding 3D quantity is ~ 1.6 .
4. For each of the alloys investigated here, an effective diffusivity whose value lies between 0.6 and 1.5 times that for impurity diffusion of chromium in nickel can be used to provide estimates of the coarsening rate. The principal exception to this finding appears to be those cases comprising a volume fraction of precipitate greater than or equal to ~ 0.6 at which the volume-fraction function may not be applicable and/or particle coalescence effects have to be considered.

5. For PM nickel-base superalloys (LSHR, Alloy 10, IN-100, Rene 88) containing greater numbers of elements, the modified LSW analysis (incorporating all solutes) with an effective diffusivity of ~ 0.5 to 1.0 times that for impurity diffusion of chromium in nickel provides reasonable estimates of coarsening rates except for temperatures below ~ 1073 K (800 °C). In this latter regime, a mechanism other than that based on bulk diffusion appears to be rate limiting.

ACKNOWLEDGMENTS

This work was conducted as part of the in-house research of the Metals Branch of the Air Force Research Laboratory's Materials and Manufacturing Directorate and the Advanced Metallic Materials Branch of the NASA Glenn Research Center. The yeoman assistance of T.M. Brown, R.E. Turner, and C.P. Lingane in conducting the experiments is gratefully acknowledged. Two of the authors (NCL, ARCG) were supported under the auspices of Contract FA8650-15-D-5230.

REFERENCES

1. M. J. Donachie (ed.): *Superalloys: Source Book*, ASM International, Materials Park, OH, 1984.
2. M. Soucail and Y. Bienvenu: *Mater. Sci. Eng. A*, 1996, vol. A220, pp. 215–22.
3. J. Cormier, X. Milhet, and J. Mendez: *J. Mater. Sci.*, 2007, vol. 42, pp. 7780–86.
4. R. Giraud, Z. Hervier, J. Cormier, G. Saint-Martin, F. Hamon, X. Milhet, and J. Mendez: *Metall. Mater. Trans. A*, 2013, vol. 44A, pp. 131–46.
5. F. Masoumi, M. Jahazi, D. Shahriari, and J. Cormier: *J. Alloys Compd.*, 2016, vol. 658, pp. 981–95.
6. M.J. Whelan: *Metal Sci. J.*, 1969, vol. 3, pp. 95–97.
7. H.B. Aaron and G.R. Kotler: *Metall. Trans.*, 1971, vol. 2, pp. 393–408.
8. H.B. Aaron and G.R. Kotler: *Metal Sci. J.*, 1970, vol. 4, pp. 222–25.
9. G. Wang, D.S. Xu, N. Ma, N. Zhou, E.J. Payton, R. Yang, M.J. Mills, and Y. Wang: *Acta Mater.*, 2009, vol. 57, pp. 316–25.
10. R.D. Doherty: in *Physical Metallurgy*, R.W. Cahn and P. Haasen, eds., North-Holland, Amsterdam, 1996.
11. D. Turnbull: in *Solid-State Physics*, F. Seitz and D. Turnbull, eds., Academic Press, New York, 1958, vol. 3, pp. 226–306.
12. A. Kelly and R.B. Nicholson: *Prog. Mater. Sci.*, 1963, vol. 10, pp. 151–391.
13. K.C. Russell: *Phase Transformations*, Metals Park, OH, ASM, 1970, pp. 219–68.
14. J.W. Christian: *The Theory of Transformations in Metals and Alloys*, 2nd ed., Pergamon Press, Oxford, 1975.
15. K.C. Russell: *Adv. Colloid Interface Sci.*, 1980, vol. 13, pp. 205–318.
16. P. Haasen, V. Gerold, R. Wagner, and M.F. Ashby: *Decomposition of Alloys: The Early Stages*, Pergamon Press, Oxford, 1984.
17. H.I. Aaronson and F.K. LeGoues: *Metall. Mater. Trans. A*, 1992, vol. 23A, pp. 1915–45.
18. H.S. Carslaw and J.C. Jaeger: *Conduction of Heat in Solids*, Oxford University Press, London, 1959.
19. H.B. Aaron, D. Fainstein, and G.R. Kotler: *J. Appl. Phys.*, 1970, vol. 41, pp. 4404–10.

20. J.W. Martin, R.D. Doherty, and B. Cantor: *Stability of Microstructure in Metallic Systems*, Cambridge University Press, Cambridge, 1997.
21. I.M. Lifshitz and V.V. Slyozov: *J. Phys. Chem. Solids*, 1961, vol. 19, pp. 35–51.
22. C. Wagner: *Zeit. Elektrochem.*, 1961, vol. 65, pp. 581–91.
23. L. Ratke and P.W. Voorhees: *Growth and Coarsening—Ostwald Ripening in Material Processing*, Springer Verlag, Berlin, 2002.
24. A.J. Ardell: *Acta Metall.*, 1972, vol. 20, pp. 61–71.
25. A.D. Brailsford and P. Wynblatt: *Acta Metall.*, 1979, vol. 27, pp. 489–97.
26. P.W. Voorhees and M.E. Glicksman: *Acta Metall.*, 1984, vol. 32, pp. 2001–11.
27. P.W. Voorhees and M.E. Glicksman: *Acta Metall.*, 1984, vol. 32, pp. 2013–30.
28. H.A. Calderon, P.W. Voorhees, J.L. Murray, and G. Kostorz: *Acta Metall. Mater.*, 1994, vol. 42, pp. 991–1000.
29. A. Umantsev and G.B. Olson: *Scripta Metall. Mater.*, 1993, vol. 29, pp. 1135–40.
30. J.E. Morral and G.R. Purdy: *Scripta Metall. Mater.*, 1994, vol. 30, pp. 905–08.
31. C.J. Kuehmann and P.W. Voorhees: *Metall. Mater. Trans. A*, 1996, vol. 27A, pp. 937–43.
32. A. Baldan: *J. Mater. Sci.*, 2002, vol. 37, pp. 2379–2405.
33. V. Biss and D.L. Sponseller: *Metall. Trans.*, 1973, vol. 4, pp. 1953–60.
34. P.K. Footner and B.P. Richards: *J. Mater. Sci.*, 1982, vol. 17, pp. 2141–53.
35. H. Li, L. Zuo, X. Song, Y. Wang, and G. Chen: *Rare Metals*, 2009, vol. 28 (2), pp. 197–201.
36. E.H. van der Molen, J.M. Oblak, and O.H. Kriege: *Metall. Trans.*, 1971, vol. 2, pp. 1627–33.
37. A.A. Hopgood and J.W. Martin: *Mater. Sci. Technol.*, 1986, vol. 2, pp. 543–46.
38. H.T. Kim, S.S. Chun, X.X. Yao, Y. Fang, and J. Choi: *J. Mater. Sci.*, 1997, vol. 32, pp. 4917–23.
39. A. Ges, O. Fornaro, and H. Palacio: *J. Mater. Sci.*, 1997, vol. 32, pp. 3687–91.
40. A. Ges, O. Fornaro, and H. Palacio: *Mater. Sci. Eng. A*, 2007, vol. A458, pp. 96–100.
41. J. Lapin, M. Gebura, T. Pelachova, and M. Nazmy: *Kovove Mater.*, 2008, vol. 46, pp. 313–22.
42. J.S. Tiley, G.B. Viswanathan, R. Srinivasan, R. Banerjee, D.M. Dimiduk, and H.L. Fraser: *Acta Mater.*, 2009, vol. 57, pp. 2538–49.
43. X. Li, N. Saunders, and A.P. Miodownik: *Metall. Mater. Trans. A*, 2002, vol. 33A, pp. 3367–73.
44. C. Ai, X. Zhao, J. Zhou, H. Zhang, L. Liu, Y. Pei, S. Li, and S. Gong: *J. Alloys Compd.*, 2015, vol. 632, pp. 558–62.
45. M. Mroczek and E. Nembach: *Acta Mater.*, 2008, vol. 56, pp. 150–54.
46. J. Coakley, H. Basoalto, and D. Dye: *Acta Mater.*, 2010, vol. 58, pp. 4019–28.
47. R.V. Miner: *Metall. Mater. Trans. A*, 1997, vol. 28A, pp. 1011–20.
48. J. Sosa, M. Huber, D.E. Welk, and H.L. Fraser: *IMMI*, 2014, vol. 3 (18).
49. T.M. Smith, P. Bonacuse, J. Sosa, M. Kulis, and L. Evans: *Mater. Charact.*, 2018, vol. 140, pp. 86–94.
50. A.R.C. Gerlt, R.S. Picard, A.E. Sauber, A.K. Criner, S.L. Semiatin, and E.J. Payton: *Metall. Mater. Trans. A*, 2018, vol. 49A, pp. 4424–28.
51. S.L. Semiatin, F. Zhang, R. Larsen, L.A. Chapman, and D.U. Furrer: *IMMI*, 2016, vol. 5 (3).
52. C.K. Sudbrack, R.D. Noebe, and D.N. Seidman: *Acta Mater.*, 2007, vol. 55, pp. 119–30.
53. S.L. Semiatin, B.C. Kirby, and G.A. Salishchev: *Metall. Mater. Trans. A*, 2004, vol. 35A, pp. 2809–19.
54. M.S.A. Karunaratne, D.C. Cox, P. Carter, and R.C. Reed: in *Superalloys 2000*, T.M. Pollock, R.D. Kissinger, R.R. Bowman, K.A. Green, M. McLean, S. Olson, and J.J. Schirra, eds., TMS, Warrendale, PA, 2000, pp. 263–272.
55. C.E. Campbell: *J. Phase Equilib. Diffus.*, 2004, vol. 25, pp. 6–15.
56. R.A. MacKay and M.V. Nathal: *Acta Metall. Mater.*, 1990, vol. 38, pp. 993–1005.
57. D.A. Grose and G.S. Ansell: *Metall. Mater. Trans. A*, 1981, vol. 12A, pp. 1631–45.
58. T.P. Gabb, J. Gayda, D.F. Johnson, R.A. MacKay, R.B. Rogers, C.K. Sudbrack, A. Garg, I.E. Locci, S.L. Semiatin, and E. Kang: “Comparison of γ - γ' Phase Coarsening Response of Three Powder Metal Disk Superalloys”, Report NASA/TM-2016-218936, NASA Glenn Research Center, Cleveland, OH, 2016.
59. A.J. Ardell and V. Ozolins: *Nat. Mater.*, 2005, vol. 4, pp. 309–16.

Publisher's Note Springer Nature remains neutral with regard to jurisdictional claims in published maps and institutional affiliations.